TRIADIC NONLINEAR INTERACTIONS AND ACOUSTICS OF FORCED VERSUS UNFORCED TURBULENT JETS

Akhil Nekkanti
Department of Mechanical and Aerospace Engineering
University of California San Diego
CA 92093, USA
aknekkan@eng.ucsd.edu

Igor Maia
Département Fluides, Thermique, Combustion
Institut PPRIME, CNRS – Université de Poitiers
86036 Poitiers, France
igor.albuquerque.maia@univ-poitiers.fr

Peter Jordan
Département Fluides, Thermique, Combustion
Institut PPRIME, CNRS – Université de Poitiers
86036 Poitiers, France
peter.jordan@univ-poitiers.fr

Liam Heidt
Division of Engineering and Applied Science
California Institute of Technology
Pasadena, CA 91125, USA
lheidt@caltech.edu

Tim Colonius
Division of Engineering and Applied Science
California Institute of Technology
Pasadena, CA 91125, USA
colonius@caltech.edu

Oliver T. Schmidt
Department of Mechanical and Aerospace Engineering
University of California San Diego
CA 92093, USA
oschmidt@eng.ucsd.edu

Abstract

We explore the potential of bispectral mode decomposition (BMD) for physical discovery in jet flows. BMD is a modal decomposition that is tailored to the extraction of flow structures involved in triadic interactions. Large-eddy simulations (LES) of turbulent forced and unforced round jets at $Re = 50,000$ and $M_j = 0.4$ are conducted and validated with the companion experiment at the Institut Pprime. The comparative BMD analysis reveals that triadic interactions in both forced and unforced jets are most prevalent in a well-defined region near and downstream of the closure of the potential core. A BMD analysis of far-field pressure sheds light on the previously reported observation that difference-interactions are more efficient radiators of jet noise than the sum-interactions.

Introduction

The reduction of jet noise is an important objective for the aviation community. The pioneering work by Crow & Champagne (1971) identified the presence of large-scale coherent structures in turbulent jets, and these coherent structures or wavepackets are the prime sources of aft-angle noise (Jordan & Colonius, 2013). A potential strategy to reduce jet noise is to perform closed-loop control that attenuates the acoustic radiation from the wavepackets. With this objective in mind, first, we harmonically force the jet to gain an understanding of the alternation of dynamics in forced jets. The forcing increases the amplitude of the wavepackets above the background turbulence. Recently, the experimental closed-loop control of turbulent jets has demonstrated the attenuation of amplified wavepackets over a broad range of frequencies (Maia *et al.*,

2020, 2021*b*, 2022). Once a strategy is designed to control the elevated wavepackets, it can be applied to a more realistic scenario of an unforced jet to reduce jet noise.

Following Crow & Champagne (1971), harmonically-forced jets has been the subject of numerous studies. The actuation of the jet has varied over a wide range of frequencies and forcing amplitudes. Most of these studies have focussed on two mechanisms that lead to the formation of coherent structures. One is the shear-layer mode or the Kelvin-Helmholtz instability, the frequency at which the shear layer rolls up into vortices. The other is the preferred mode or the jet column mode (Hussain & Zaman, 1981), characterized by the frequency at which the jet exhibits the greatest response to external forcing. At low amplitudes of forcing, the jets exhibit a linear response. As the forcing amplitude increases, it triggers nonlinear interactions in jets. High levels of forcing and the resulting nonlinear interactions of coherent structures have rarely been explored. Raman & Rice (1991); Husain & Hussain (1995); Broze & Hussain (1994); Shaabani-Ardali *et al.* (2019) have investigated the nonlinear response to high amplitude forcing in jets, and most have focussed on initially-laminar jets. In this work, nonlinear interactions in unforced and forced jets are examined and compared for turbulent jets. Here, we perform LES of unforced and forced turbulent subsonic jets at a Reynolds number, $Re = \rho_j U_j D / \mu_j = 50,000$, and Mach number, $M = U_j / c_\infty = 0.4$, where ρ is the density, U the mean flow velocity, μ the dynamic viscosity, c the speed of sound, and the subscripts j and ∞ denote the jet and free-stream conditions. We validate our simulations with the experiments performed at Institut Pprime. Following the experiments, the jets are forced harmonically at a non-dimensional frequency of $St = fD/U_j = 0.4$, near the nozzle lip.

Bispectral mode decomposition

In this study, we use the bispectral mode decomposition (BMD), recently proposed by Schmidt (2020), to investigate the triadic interactions triggered by the axisymmetric excitation of the jet. BMD is a technique that can be understood as an extension of classical bispectral analysis to multidimensional and multivariate data. The bispectrum is defined as the double Fourier transform of the third moment of a time signal. For a time series, $y(t)$ with zero mean, the bispectrum is

$$S_{yyy}(f_1, f_2) = \int\int R_{yyy}(t_1, t_2)e^{-i2\pi(f_1\tau_1 + f_2\tau_2)}d\tau_1 d\tau_2, \quad (1)$$

where $R_{yyy}(\tau_1, \tau_2) = E[y(t)y(t-\tau_1)y(t-\tau_2)]$ is the third moment of $y(t)$, and $E[\cdot]$ is the expectation operator. The bispectrum is a signal processing tool for one-dimensional time series which only measures the quadratic phase coupling locally. On the contrary, BMD is a modal decomposition technique that identifies the spatially coherent structures associated with the triadic interactions.

For a fluctuating flow field $\mathbf{q}_i = \mathbf{q}(x, t_i)$, where $i = 1, 2, \cdots n_t$, BMD maximizes the integrated point-wise bispectrum

$$b(f_k, f_l) = E\left[\int_\Omega \hat{\mathbf{q}}^*(x, f_k) \circ \hat{\mathbf{q}}^*(x, f_l) \circ \hat{\mathbf{q}}(x, f_k + f_l)dx\right]. \quad (2)$$

Here, $\hat{\mathbf{q}}$ is the temporal Fourier transform of $\mathbf{q}$ computed using the Welch approach (Welch, 1967), Ω is the spatial domain of interest, $(\cdot)^*$ denotes the complex conjugate, and $\circ$ denotes the Hadamard (or element-wise) product.

Next, all the Fourier realizations at frequency f_k are arranged into a matrix, $\hat{\mathbf{Q}}_k = \left[\hat{\mathbf{q}}_k^{(1)}, \hat{\mathbf{q}}_k^{(2)}, \cdots, \hat{\mathbf{q}}_k^{(n_{blk})}\right]$. The auto-bispectral matrix is then computed as

$$\mathbf{B} = \frac{1}{n_{blk}}\hat{\mathbf{Q}}_{k\circ l}^H \mathbf{W}\hat{\mathbf{Q}}_{k+l}, \quad (3)$$

where $\hat{\mathbf{Q}}_{k\circ l}^H = \hat{\mathbf{Q}}_k^* \circ \hat{\mathbf{Q}}_l^*$ and $\mathbf{W}$ is the diagonal matrix containing the spatial quadrature weights. Owing to the non-Hermitian nature of the bispectral matrix, we obtain the complex mode bispectrum by solving the optimization problem

$$\lambda_1(f_k, f_l) = \arg\max\left|\frac{\mathbf{a}_1^*\mathbf{B}\mathbf{a}_1}{\mathbf{a}_1^*\mathbf{a}_1}\right|, \quad (4)$$

for the optimal expansion coefficients $\mathbf{a}_1$, by determining the numerical range of $\mathbf{B}$. For further details on computing the mode bispectrum, the reader is referred to Schmidt (2020). Finally, the bispectral modes are recovered as

$$\phi_{k+l}^{(1)} = \hat{\mathbf{Q}}_{k+l}\mathbf{a}_1. \quad (5)$$

Validation of LES

The experiments of the isothermal subsonic jets were performed at the "JET100" low Mach number jet facility at Institut PPRIME, Poitiers, France. The experiments were carried out for a jet Mach number $M_j = 0.05$, and Reynolds number of $Re = 50000$. The boundary layer is tripped inside the nozzle by a carborundum strip located $2.5D$ upstream from the nozzle exit. The turbulent jet is forced by eight loudspeakers that are equally distributed around the nozzle lipline ($r/D = 0.5$). The loudspeakers generate synthetic jets through an annular gap of width $0.01D$. For further details of the experimental setup, the reader is referred to Maia *et al.* (2020, 2021*b*, 2022).

We perform large-eddy simulations of subsonic jets using the compressible flow solver "Charles" developed at Cascade Technologies Brès *et al.* (2017, 2018). Charles solves the spatially filtered compressible Navier–Stokes equations on unstructured grids using a density-based finite-volume method. The LES combines the Vreman sub-grid model (Vreman, 2004) with the wall-model by Bordat and Larsson (Bodart & Larsson, 2012; Kawai & Larsson, 2012). The reader is referred to Brès *et al.* (2017, 2018) for further details on the numerical method and validation on jet flows.

The validation of the LES case for the present case follows the previous studies. In particular, the mesh used by Brès *et al.* (2018) is modified to accommodate the new nozzle geometry and refined in the vicinity of the synthetic jet actuators. The total grid size is 16.6 million control volumes. The LES is conducted for the experimental Reynolds number, whereas the Mach number is artificially increased to $M_j = 0.4$. Effects of compressibility are still small in this regime and the very small time steps associated with the incompressible limit are avoided.

The LES results for the unforced jet are compared to the experiments in figure 1. The mean and RMS streamwise velocities on the centerline and lipline are reported in figure 1(*a,c*) and 1(*b,d*), respectively. In figure 1(*a*), the mean streamwise velocities along the centerline of the experiment and the simulation are almost indistinguishable within the first ten jet diameters. The corresponding potential core length, indirectly defined as $\bar{u}(x = x_c) = 0.95U_j$ is $x_c \approx 6.2$. The RMS velocity along the centerline, shown in figure 1(*c*), matches well for the first six jet diameters and is underpredicted by about 10% further downstream. The lipline RMS velocity in figure 1(*d*) is slightly overpredicted near the nozzle and underpredicted with a maximum deviation of also about 10% further downstream. Clearly visible in the simulation results are grid transitions that were similarly observed by Brès *et al.* (2018). It was confirmed in the same work that increasing the resolution mitigates these transitions. More importantly, Brès *et al.* (2018) also showed that both nozzle-exit turbulent statistics and far-field noise predictions were accurate for the lower resolution simulations that exhibit grid transitions.

For the forced simulation, we follow Heidt *et al.* (2021) and model the effect of the loudspeaker actuators as an acoustic forcing in the annular region along the lip line, $0.50 \leq r \leq 0.51$, as

$$
\begin{aligned}
p(r) &= 1 - 40000(r - 0.505)^2, \\
u_x(r,t) &= Ap(r)\sin(2\pi St_f t), \\
u_r &= u_\theta = 0, \\
\rho &= \rho_\infty + \rho_\infty u_x/c_\infty, \\
p &= p_\infty + \rho_\infty c_\infty u_x.
\end{aligned}
$$

The amplitude, A, was manually adjusted to match the experimental observations. Here, $St_f = 0.4$ is the forcing frequency. Figure 2 shows the power spectral densities of the centerline streamwise velocity at $x = 2$ for the unforced and forced jets. The comparison between experiment and simulation are excellent for the unforced jet seen in figure 2(*a*). The best agreement for the forced case was obtained for $A = 0.4$ and is shown in
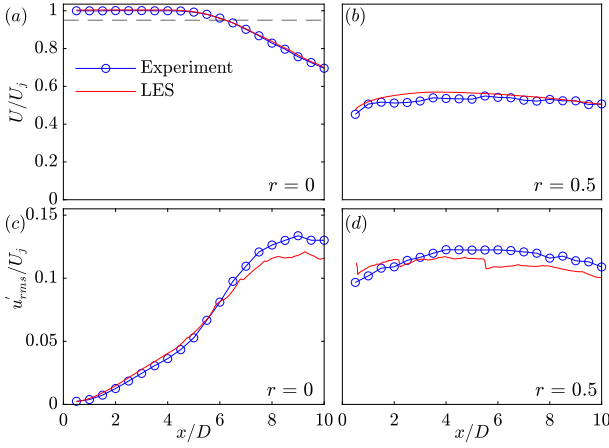
Figure 1. Comparison of the experiment with the LES simulations: centerline (a,c) and lipline (b,d). Profiles of the mean (a,b) and (c,d) RMS streamwise velocity. Black dashed line represents $U/U_j = 0.95$ and its intersection with the mean streamwise velocity indicates the length of the potential core.
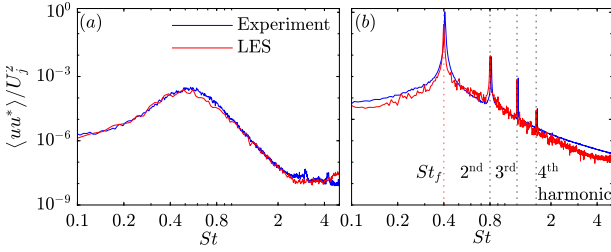

Figure 2. Power spectral density of the streamwise velocity at $x = 2$ and $r = 0$: (a) unforced jet; (b) forced jet. The experiment (blue line) is compared to the simulations (red line). $St = St_f = 0.4$ corresponds to the forcing frequency (red dotted line).

figure 2(b). Both the peaks at the forcing frequency and its harmonics, as well as the number of active harmonics and the underlying broadband spectrum, are well predicted.

Triadic interactions in forced and unforced jets

Figure 3 shows the area-integrated power spectral densities (PSD) for the five most energetic azimuthal wavenumbers $m = 0,1,2,3,4$. The PSDs are integrated over the compressible energy norm. The azimuthal wavenumber $m = 0$ contains most of the energy for the unforced and forced jets. For the forced jets, we observe large peaks at the forcing frequency and its harmonics in the wavenumber $m = 0$. The peaks at these harmonic frequencies indicates the presence of triadic sum interactions. As the other wavenumbers are not affected, we focus our analysis on the nonlinear interactions in the axisymmetric component $m = 0$.

The mode bispectra for the unforced and forced jets are shown in figure 4. The high-intensity regions (false red color) in the mode bispectra signify the dominant triads that arise from the interactions of two frequencies. Different combinations of frequencies (St_1,St_2) interact to generate the same frequency $(St_1 + St_2 = \text{constant})$ along the diagonals of slope -1 in the mode bispectrum. For the forced jet (figure 4 (b)), a grid-like pattern is observed with vertical, horizontal, and diagonal lines at the forcing frequency and its harmonics with local
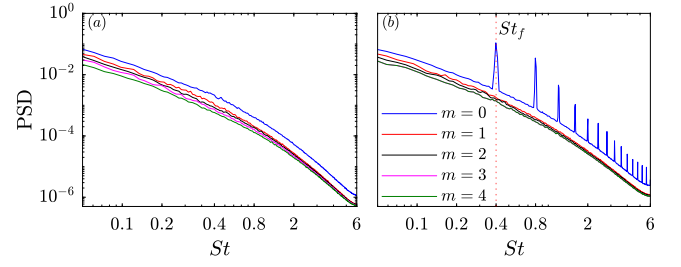

Figure 3. Integrated PSD of first five azimuthal wavenumbers, $m = 0,1,2,3,4$ for the two jets: (a) unforced turbulent; (b) forced turbulent jet. PSD is integrated over the compressible energy norm.
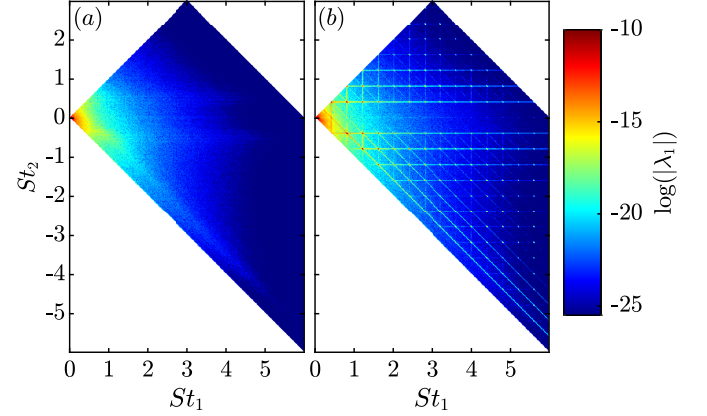

Figure 4. BMD spectra: (a) unforced turbulent; (b) forced turbulent jet.

maxima at the intersection of these lines. These local maxima represent the prominent triadic interactions. In particular the two most dominant triads are (0.4,0.4,0.8) and (0.8,-0.4,0.4). In the case of unforced jets, a broadband behavior is observed, with the highest values concentrated at lower frequencies.

Next, we examine the mode bispectrum along different diagonals with $St_3 = \text{const}$ to identify the strongest non-linear interaction that result in a triad at each frequency. Figure 5 shows the mode bispectrum along the constant frequencies of $St_3 = 0.0, 0.4, 0.8$, and 1.2 for the two cases. The spectrum of the unforced jet is broadband for all St_3. The forced jet exhibits distinct peaks at the forcing frequency and its harmonics. The two most dominant triads are observed for $St_3 = 0.4$ in figure 5(b) and $St_3 = 0.8$ in 5(c). The first of these two triads is the difference interaction between $St_1 = 2St_f$ and $St_2 = -St_f$, i.e., between the second harmonic and the conjugate forcing frequency. The second triad is the fundamental self-interaction, $(St_f,St_f,2St_f)$, that creates the second harmonic. The dips of the forced mode bispectrum observed for $St_2 = 0$ in figure 5(b), (c), and (d) correspond to the relative lower values of the mode bispectrum previously seen along the abscissa in figure 4(b). Note that the zero-frequency bin contains unresolved low frequency components due to the finite sampling frequency, and the non-zero mode bispectrum should not be interpreted along $St_2 = 0$.

The BMD modes of the triad cascade including the most significant interactions up to $St_1 \leq 2St_f$ are visualized in figure 6. The cascade starts with the mode at the forcing frequency, ϕ_{St_f+0} (left column middle row). The modes associated with the sum interactions are shown in the first and second row, and those associated with the difference interactions are shown in
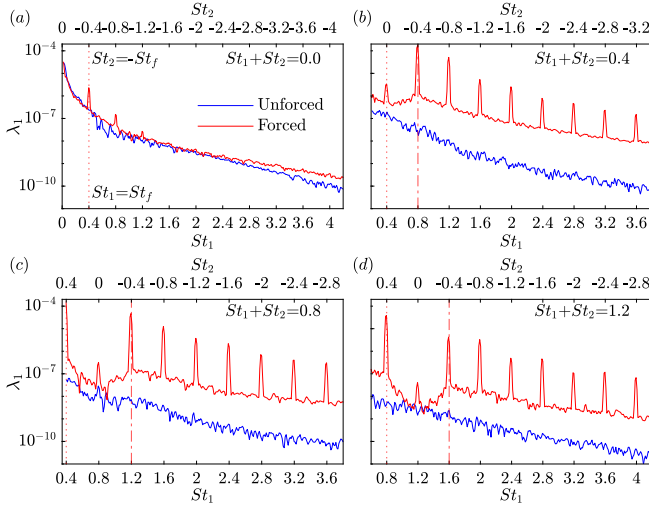
Figure 5. Mode bispectrum along diagonal of constant frequency: (*a*) $St_3 = St_1 + St_2 = 0.0$; (*b*) $St_3 = St_1 + St_2 = 0.4$; (*c*) $St_3 = St_1 + St_2 = 0.8$; (*d*) $St_3 = St_1 + St_2 = 1.2$. The red dotted and dash-dotted lines denote the forcing, and conjugate forcing frequency, respectively.
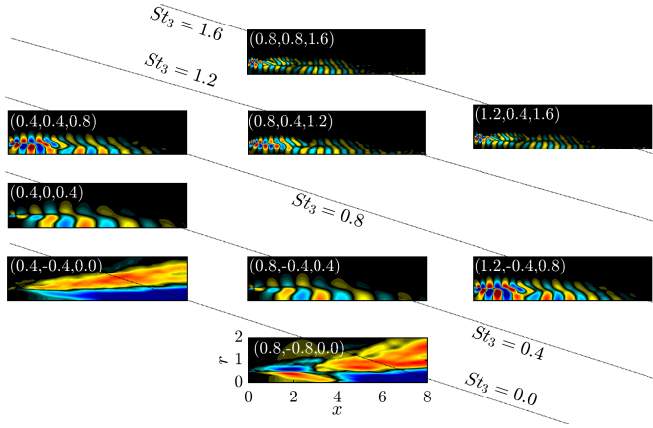

Figure 6. Bispectral modes forming a cascade of triads, starting from the forcing frequency (St_1,St_2,St_3) = (0.4,0.0,0.4), middle-left. The real part of the streamwise velocity component is shown.

the fourth and fifth row. The mode ϕ_{St_f+0} self-interacts to generate the second harmonic, $\phi_{St_f+St_f}$. The fundamental forcing mode and its second harmonic then interact to create the third harmonic, $\phi_{2St_f+St_f}$, and so on. In the negative St_2 plane, the destructive self interaction of the forcing mode creates a mean flow distortion mode, $\phi_{St_f+-St_f}$, with $St_3 = 0$. Inspecting the modes reveals that sum-interactions create modes with high wavenumbers and difference-interactions create modes with lower streamwise wavenumbers. This behaviour is in agreement with the linear dispersion relation of these Kelvin-Helmholtz (KH) type instability waves.

Another interesting observation is that the spatial structures of the modes along the diagonals of constant frequencies $St_3 = 0.4$, 0.8, 1.2 and 1.6 are very similar. As shown for the companion experiment by Maia *et al.* (2021*a*), these similar bispectral modes at constant $St_3 \neq 0$ resemble the leading SPOD modes at each frequency. This indicates that the spatial structures created by the triadic interactions are also the most energetic coherent structures. Along $St_3 = 0$, on the contrary,
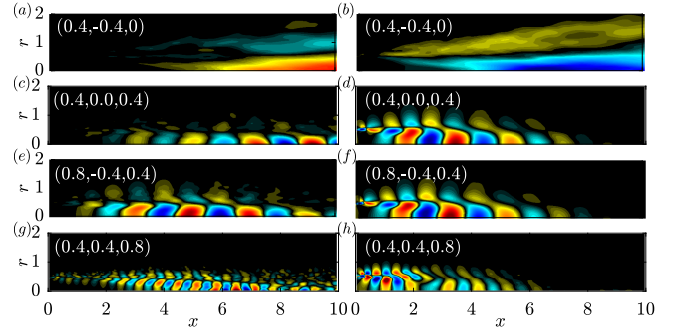

Figure 7. Streamwise velocity component of the BMD modes for the turbulent unforced (*a,c,e,g*) and forced jets (*b,d,f,h*) for different frequency triads: (*a,b*) (St_f,-St_f,0); (*c,d*) (St_f,0,St_f); (*e,f*) (2St_f,−St_f,St_f); (*g,h*) (St_f,St_f,2St_f).
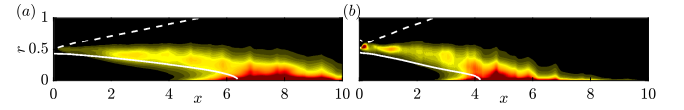

Figure 8. Integral interaction maps, $\sum_{k,l} \lambda_1(St_k,St_l)|\phi_{k\circ l} \circ \phi_{k+l}|$: (*a*) unforced turbulent jet; (*b*) forced turbulent jet. White solid and dashed lines outline the potential core and the jet width defined as lines of constant $u_x = 0.95U_j$ and $0.05U_j$, respectively.

the streak-like structures with an increasing number of streamwise lobes are created by the destructive self-interactions of the forcing mode and its harmonics.

Next, we compare the spatial structures of the BMD modes associated with the triadic interactions for unforced and forced turbulent jets. Figure 7 shows the streamwise velocity components for the dominant triads at (St_f,-St_f,0), (St_f,0,St_f), (2St_f,−St_f,St_f), and (St_f,St_f,2St_f), which correspond to the mean flow deformation, fundamental instability mode, a harmonic-fundamental difference interaction and fundamental self-interaction, respectively. The BMD modes reveal that the structures contributing to the triadic interactions are localized to the region near the end of the potential core for the unforced jet, whereas, for the forced jet, they are located at a more upstream location and are concentrated in the shear layer. This effect is more pronounced for the BMD mode of the fundamental self-interaction triad (St_f,St_f,2St_f), which exhibits a KH type wavepacket near the nozzle exit in the forced jet.

We next seek to identify the regions where triadic interactions are most active. This is achieved by summing the weighted interaction maps over all frequency triads as $\sum_{k,l} \lambda_1(St_k,St_l)|\phi_{k\circ l} \circ \phi_{k+l}|$. The resulting integral interaction maps are presented in figure 8 and indicate the regions where the triadic interactions are most active. Both jets exhibit strong triadic nonlinear interactions downstream of the potential core near the centerline. This observation is in agreement with previous findings by Cavalieri *et al.* (2013) and Tissot *et al.* (2017), who, in the same region, observed that linear wavepacket models differ significantly from experiments. In addition to this 'natural' occurrence of nonlinear effects, the forced jet interaction map also reveals the presence of strong nonlinearity in the shear layer near the nozzle exit that is directly associated with the forcing. Also observed is a shortening of the potential core and a thickening of the shear layer. This is in agreement with the previous works by Crow &
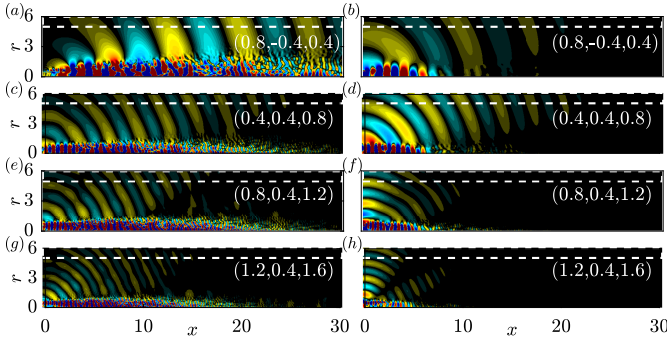
Figure 9. BMD modes of the pressure field for the turbulent unforced (*a,c,e,g*) and forced jets (*b,d,f,h*) for different frequency triads: (*a,b*) $(2St_f, -St_f, St_f)$; (*c,d*) $(St_f, St_f, 2St_f)$; (*e,f*) $(2St_f, St_f, 3St_f)$; (*g,h*) $(3St_f, St_f, 4St_f)$.

Champagne (1971); Samimy *et al.* (2007), who argue that the enhanced entrainment due to forcing leads to a widening of the shear layer, and consequently, a contraction of the potential core.

To identify the link between the triadic interactions in the near-field and the acoustic far-field, we perform BMD on the pressure data using a weight matrix,

$$\mathbf{W}_{ac}(x) = \begin{cases} 1 \text{ for } 5 \leq r \leq 6, \forall x \in \Omega \\ 0 \text{ otherwise,} \end{cases} \qquad (6)$$

that focuses on the far-field. Figure 9 shows the BMD modes for the resultant frequencies (St_3) of St=0.4 (*a,b*), 0.8 (*c,d*), 1.2 (*e,f*) and 1.6 (*g,h*). The BMD mode corresponding to the most dominant triad at each resultant frequency (St_3) is selected. The pressure components for the unforced and forced turbulent jets are shown in figure 9 (*a,c,e,g*) and 9 (*b,d,f,h*) respectively. In case of the forced jet, $(2St_f, -St_f, St_f)$ is the most significant triad identified from the BMD spectra (not shown here). This identifies as the difference-interaction between the first harmonic and the forcing frequency and is the most significant triad. This observation is in agreement with the findings of Sandham *et al.* (2006), who show that unstable waves with difference-interactions ($St_3 = St_1 - St_2$) are more efficient radiators of jet noise than the sum-interactions ($St_3 = St_1 + St_2$). For the forced jet, the BMD modes exhibit beams that propagate at a steeper angle as compared to the unforced jet. For the triads (0.8, 0.4, 1.2) and (1.2, 0.4, 1.6), the unforced jet exhibits directive downstream radiation, whereas for the forced jet, we observe actuation-induced sideline noise. These sideline radiation patterns are similar to those found by Jeun *et al.* (2016) and Nekkanti & Schmidt (2021).

Summary and conclusions

LES of unforced and forced turbulent jets were performed and validated with companion experiments. The jet is axisymmetrically forced by blowing and suction at a frequency of $St = 0.4$ and with an amplitude that correspond to the jet velocity, triggering strong nonlinear interactions. The forcing produces a purely axisymmetric response and entails significant thickening of the shear layer and shortening of the potential core. The axisymmetric component, $m = 0$, exhibits peaks at the forcing frequency and its harmonics due to triadic interactions. BMD is employed to investigate the structures associates with these triads and their relative significance. Integral interaction maps are defined to identify regions of activity of triadic interactions. Both unforced and forced jets exhibit strong interactions in the closure region of the potential core. This 'natural' region of nonlinear activity extends over ~ 6 jet diameters in the unforced case and over ~ 4 in the forced case, respectively. We speculate that the nonlinear activity in that region is the reason for the discrepancy of SPOD modes and linear resolvent (Schmidt *et al.*, 2018) and global modes (Schmidt *et al.*, 2017), and similarly the discrepancy between linear wavepacket models and experimental data, also attested to nonlinearity by Cavalieri *et al.* (2013) and Tissot *et al.* (2017). In the forced jet, strong interactions that are associated with the large-amplitude forcing are identified in the vicinity of the actuator near the lip line. Lastly, BMD was applied to the far-field pressure and identified the difference-interaction between the first harmonic and the forcing frequency as the most significant triad. This observation is in agreement with the findings of Sandham *et al.* (2006).

REFERENCES

Bodart, J. & Larsson, J. 2012 Wall-modeling in large eddy simulation: length scales, grid resolution, and accuracy. *Annual research briefs* pp. 229–240.

Brès, G. A., Ham, F. E., Nichols, J. W. & Lele, S. K. 2017 Unstructured large-eddy simulations of supersonic jets. *AIAA Journal* pp. 1164–1184.

Brès, G. A., Jordan, P., Jaunet, V., Le Rallic, M., Cavalieri, A. V. G., Towne, A., Lele, S. K., Colonius, T. & Schmidt, O. T. 2018 Importance of the nozzle-exit boundary-layer state in subsonic turbulent jets. *J. Fluid Mech.* **851**, 83–124.

Broze, G. & Hussain, F. 1994 Nonlinear dynamics of forced transitional jets: periodic and chaotic attractors. *J. Fluid Mech.* **263**, 93–132.

Cavalieri, A. V. G., Rodríguez, D., Jordan, P., Colonius, T. & Gervais, Y. 2013 Wavepackets in the velocity field of turbulent jets. *J. Fluid Mech.* **730**, 559–592.

Crow, S.C. & Champagne, F.H. 1971 Orderly structure in jet turbulence. *J. Fluid Mech.* **48** (3), 547–591.

Heidt, L., Colonius, T., Nekkanti, A., Schmdit, O., Maia, I. & Jordan, P. 2021 Analysis of forced subsonic jets using spectral proper orthogonal decomposition and resolvent analysis. In *AIAA Aviation 2021 Forum*, p. 2108.

Husain, H.S. & Hussain, F. 1995 Experiments on subharmonic resonance in a shear layer. *J. Fluid Mech.* **304**, 343–372.

Hussain, A. K. M. F. & Zaman, K. B. M. Q. 1981 The 'preferred mode' of the axisymmetric jet. *J. Fluid Mech.* **110**, 39–71.

Jeun, J., Nichols, J. W. & Jovanović, M. R. 2016 Input-output analysis of high-speed axisymmetric isothermal jet noise. *Phys. Fluids* **28** (4), 047101.

Jordan, P. & Colonius, T. 2013 Wave packets and turbulent jet noise. *Annu. Rev. Fluid Mech.* **45**, 173–195.

Kawai, S. & Larsson, J. 2012 Wall-modeling in large eddy simulation: Length scales, grid resolution, and accuracy. *Phys. Fluids* **24** (1), 015105.

Maia, I., Jordan, P., Heidt, L., Colonius, T., Nekkanti, A. & Schmidt, O. T. 2021a Nonlinear dynamics of forced wavepackets in turbulent jets. In *AIAA Aviation 2021 Forum*, p. 2277.

Maia, I. A., Jordan, P. & Cavalieri, A. V. G. 2022 Wave cancellation in jets with laminar and turbulent boundary lay-

ers: The effect of nonlinearity. *Physical Review Fluids* **7** (3), 033903.

Maia, I. A., Jordan, P., Cavalieri, A. V. G., Martini, E., Sasaki, K. & Silvestre, F. J. 2021*b* Real-time reactive control of stochastic disturbances in forced turbulent jets. *Physical Review Fluids* **6** (12), 123901.

Maia, I. A., Jordan, P., Cavalieri, A. V. G., Martini, E. & Silvestre, F. 2020 Closed-loop control of forced turbulent jets. *arXiv preprint arXiv:2009.09299* .

Nekkanti, A. & Schmidt, O. T. 2021 Modal analysis of acoustic directivity in turbulent jets. *AIAA J.* **59** (1), 228–239.

Raman, G. & Rice, E.J. 1991 Axisymmetric jet forced by fundamental and subharmonic tones. *AIAA J.* **29** (7), 1114–1122.

Samimy, M., Kim, J. H., Kastner, J., Adamovich, I. & Utkin, Y. 2007 Active control of high-speed and high-reynolds-number jets using plasma actuators. *J. Fluid Mech.* **578**, 305–330.

Sandham, N.D., Morfey, C.L. & Hu, Z.W. 2006 Sound radiation from exponentially growing and decaying surface waves. *J. Sound Vib.* **294** (1-2), 355–361.

Schmidt, O. T 2020 Bispectral mode decomposition of nonlinear flows. *Nonlinear Dyn.* **102** (4), 2479–2501.

Schmidt, O. T., Towne, A., Colonius, T., Cavalieri, A. V. G., Jordan, P. & Brès, G. A. 2017 Wavepackets and trapped acoustic modes in a turbulent jet: coherent structure eduction and global stability. *J. Fluid Mech.* **825**, 1153–1181.

Schmidt, O. T., Towne, A.and Rigas, G., Colonius, T. & Brès, G. A. 2018 Spectral analysis of jet turbulence. *J. Fluid Mech.* **855**, 953–982.

Shaabani-Ardali, L., Sipp, D. & Lesshafft, L. 2019 Vortex pairing in jets as a global floquet instability: modal and transient dynamics. *J. Fluid Mech.* **862**, 951–989.

Tissot, G., Zhang, M., Lajús, F. C., Cavalieri, A. V. G. & Jordan, P. 2017 Sensitivity of wavepackets in jets to nonlinear effects: the role of the critical layer. *J. Fluid Mech.* **811**, 95–137.

Vreman, AW 2004 An eddy-viscosity subgrid-scale model for turbulent shear flow: Algebraic theory and applications. *Phys. Fluids* **16** (10), 3670–3681.

Welch, P. 1967 The use of fast fourier transform for the estimation of power spectra: a method based on time averaging over short, modified periodograms. *IEEE Trans. Audio Electroacoust.* **15** (2), 70–73.